Supplementary Information for:

Nanofibrous-spherical cage mimicking a ball of pearl-necklaces for super capture of heavy metal ions

Youngkyun Jung[a,b], Ung Su Choi[a,b] & Young Gun Ko[c]✉

SUPPORING INFORMATION:

1) Supplementary Methods

2) Supplementary Fig. 1 – 22

3) Supplementary Table 1 – 10

[a] Division of Energy & Environment Technology, Korea University of Science and Technology, 217 Gajeong-ro, Yuseong-gu, Daejeon, 34113, Republic of Korea. [b] National Agenda Research Division, Korea Institute of Science and Technology, Hwarang-ro 14-gil 5, Seongbuk-gu, Seoul, 02792, Republic of Korea. [c] Department of Chemical Engineering and Materials Science, Sangmyung University, Hongjimun 2-gil 20, Jongno-gu, Seoul 03016, Republic of Korea. ✉ e-mail: younggun@smu.ac.kr

Supplementary Methods

Characterizations. All synthesized materials were analyzed using a Fourier transform infrared (FT-IR) spectrometer (Frontier, PerkinElmer). X-ray photoelectron spectroscopy (XPS, PHI 5000 VersaProbe, Ulvac-PHI) analysis was also carried out with a monochromatic Al Kα X-ray source (1486.6 eV of photons, 15 kV and 25 W) to investigate the unclearly assigned peaks in FT-IR spectra of samples. All binding energies of obtained data were referenced to the neutral C1s peak at 285.0 eV to compensate for the surface-charging effects. The peaks were deconvoluted using a curve-fitting method with the software of CasaXPS (version 2.3.12). The thermal stability of the NFC adsorbent was investigated using thermogravimetric analysis (TGA, TGA Q500, TA Instrument, USA). The morphology of samples and size distribution of spheres were characterized using a scanning electron microscope (SEM, Inspect F50, FEI). Grown crystals in the NFC adsorbents were observed using a high-resolution transmission electron microscope (HR-TEM, Technai F20, FEI) operating at 200 kV. X-ray diffraction (XRD) patterns of crystal samples were recorded using a Rigaku Dmax 2500 with a Cu Kα source (40 kV and 200 mA). The XRD patterns data were analyzed by MDI Jade 5.0 software (Materials Data Inc.). The surface area and porosity of porous samples were characterized by the Brunauer-Emmett-Teller (BET) method based on adsorption isotherms of nitrogen gas (ASAP2420 sorption analyzer, Micromeritics) and mercury intrusion porosimetry (MicroActive AutoPore V 9600, Micromeritics). The compressive strength of the NFC adsorbent was evaluated with a table top mechanical tester (Instron 3345, single column system, Instron) at a constant cross-head speed of 10 mm/min. The concentration of metal ions in aqueous solution was determined by an inductively coupled plasma optical emission spectroscope (ICP-OES, 710-ES, Varian).

Synthesis of polyacrylonitrile nanoparticle (PAN-NP). PAN-NP was synthesized using a mixture solution I (deionized (120 g, DI) water (Millipore Milli-Q water system, 18.2 MΩ/cm), sodium dodecyl sulfonate (0.50 g, SDS, Sigma Aldrich, ≥99%), and potassium persulfate (0.16 g, KPS, Sigma Aldrich, ≥99%)) and a mixture solution II (DI water (40 g), acrylonitrile (40 g, AN, Sigma Aldrich, ≥99%), poly(ethylene glycol) 4-nonylpenyl 3-sulfopropyl ether potassium salt (0.58 g, NP-PEG-SO$_3$K, Sigma Aldrich), and SDS (0.53 g)). The solution I was put into 500 ml round-bottom flask with stirring for 30 min. And then, the polymerization was carried out with stirring at 400 rpm under N$_2$ purging for 4 h at 70 °C after pouring the solution II into the prepared solution I. The synthesized PAN-NP was washed with water, separated using a high speed centrifuge (Hanil, SUPRA 21K) at 8000 rpm for 20 min, and finally dried using a freeze drier (5 mTorr, Ilshin Co., FD5508,) for 1 week.

Surface modification of PAN-NP with diethylenetriamine. PAN-NPs (30 g) was swollen in diethylenetriamine (200 mL, DETA, Sigma Aldrich, 99%) for 30 min in a 500 mL round-bottom flask for the formation of thick aminated-layer on the surface of PAN-NPs, followed by adding boron trifluoride dihydrate (0.3 g, BF$_3$·2H$_2$O, Sigma Aldrich, 96%) as non-metal based Lewis acid catalyst. Sunsequently, the mixture was maintained for 2 h at 110 °C with stirring at 200 rpm. The synthesized yellowish solids were denoted as aminated PAN-NP (APAN-NP). The APAN-NP was washed with excess DI water, 1 N HCl solution (Sigma Aldrich), 1 N NaOH solution (Sigma

Aldrich) and DI water in that order to remove unreacted DETA, and then filtered with a 0.45 μm pore size filter (MF-Millipore Membrane Filter, Merck). The obtained particles were dried using a freeze drier for 1 week.

Preparation of nanofibrous-spherical cage (NFC) adsorbents. 0.5 wt% sodium alginate (Na-Alg, Sigma Aldrich) solution was prepared by dissolving Na-Alg in DI water with stirring. The stable dispersion of a APAN-NPs mixture was made by the addition of APAN-NPs (10 g) in 0.5 wt% Na-Alg solution (90 g), followed by POWERSONIC 405 (Hwashin Instrument Co.) ultrasonication. To fabricate NFC structure composed of the APAN-NPs and binders, an extrusion/external gelation method was used by continuously dropping the APAN-NPs dispersed Na-Alg solution into 2 N calcium chloride solution (CaCl$_2$, Sigma Aldrich, ≥97.0%) solution with a nozzle (nozzle diameter = 2 mm; distance between the end of the nozzle and the surface of Ca^{2+} solution = 50 mm). The continuously mass-produced APAN-NPs/Ca-Alg spherical hydrogels kept in the aqueous Ca^{2+} solution with stirring at 200 rpm for 3 h, and then were washed with water and ethanol. The hydrogel was frozen to -80°C in the rapid refrigeration (Ilshin, DF9010) followed by freeze-drying using a freeze drier for 1 week for preventing the change of NFC volume by swelling with water. The content of APAN-NPs in the prepared NFC adsorbent was calculated by:

$$APAN - NP \ content \ of \ adsorbent \ (wt\%) = \frac{100 m_A w_n}{m_n w_c + m_A w_n}$$

(1)   where m_n and m_A indicate the weights of the used Na-Alg and APAN-NP, respectively. And w_n and w_c are molecular weight of the Na-Alg and Ca-Alg, respectively.

Single-component batch sequestration experiments. The stock solutions of heavy metal ions were prepared by dissolving metal nitrate (Pb(NO$_3$)$_2$, Cd(NO$_3$)$_2$·4H$_2$O, and Cu(NO$_3$)$_2$·3H$_2$O, Sigma Aldrich, ≥99.0%) in DI water. All sequestration tests were conducted at room temperature. In a typical run, the effects of adsorbent dose, pH value of solution, adsorption-desorption cycle, sequestration time, and initial concentration of heavy metal ions on the sequestration performance of NFC adsorbent were investigated. For each sequestration test, at least five replicates were carried out and averaged.

q_e (sequestration capacity adsorbed at equilibrium, mg/g), representing the adsorbed amount (mg) per unit mass of adsorbent (g), was calculated by below Eq. (1):

$$q_e = \frac{(C_i - C_e) \times V}{M}$$

(1)

where C_i and C_e (mg/L) are the initial and equilibrium concentration, respectively. V is the volume of the solution (L), and M is the mass of the adsorbent (g).

The removable efficiency ($Re\%$) was calculated by Eq. (2):

$$Re\% = \frac{C_i - C_e}{C_i} \times 100$$

(2)

Effect of dose on sequestration capacity of NFC adsorbents. Different dose of the NFC adsorbent was added into a glass bottle containing 0.05 L stock solution with the concentration of 100 ppm for each heavy-metal ions (Pb^{2+}, Cd^{2+}, and Cu^{2+}). pH of the solution was not adjusted. The mixtures were kept with agitation at 200 rpm for 24 h and filtered through 0.45-μm-pore membrane filter. Consequently, the residual heavy metal contents in the solution were determined by using ICP-OES.

Effect of pH on sequestration **capacity of NFC.** NFC dose of 1.0 g/L was added into a glass bottle containing each heavy-metal solution with 100 ppm C_i. pH in the solution was adjusted in a range of between 2 and 8 by using 1 N HNO_3 and diluted NH_4OH solution. The mixture was kept with agitation at 200 rpm for 24 h and filtered through 0.45-μm-pore membrane filter. Then, the residual metal content in the solution was determined by using ICP-OES.

Effect of adsorption-desorption cycle on sequestration capacity of NFC. The removal process was carried out by adding of NFC (0.05 g) in a heavy metal ion solution (0.05 L, C_i = 100 ppm), filtered through 0.45-μm-pore membrane filter. pH of the solution was not adjusted. The NFC was regenerated by being treated for 24 h each in 1 N HNO_3 and saturated calcium hydroxide (($Ca(OH)_2$, Sigma Aldrich, ≥95.0%) solution. The regeneration process was repeated for 15 cycle. The mixture was kept with agitation at 200 rpm for 24 h and filtered through 0.45-μm-pore membrane filter. Then, the residual metal content in the solution was determined by using ICP-OES.

Adsorption isotherm studies. NFC (0.05g) was put into a glass bottle containing a stock solution (0.05 L) of each three heavy metal ions with change of C_i, and pH of the solution was not adjusted. And then the mixture was kept with agitation at 200 rpm for 24 h and filtered through 0.45-μm-pore membrane filter. Then, the residual heavy metal ion content in the solution was determined by using ICP-OES. The three representative adsorption isotherm models were fitted with the equilibrium sequestration data.

The Langmuir model is based on the assumption that (a) all the adsorption sites have an identical binding energy, (b) each site binds to only a single adsorbate in a monolayer, and (c) interaction between the adsorbed molecules is not generated. The Langmuir isotherm model is defined as:

$$q_e = \frac{q_m K_L C_e}{1 + K_L C_e}$$

(3)

where q_m (mg/g) and K_L (L/mg) is the maximum sequestration capacity of heavy metal ions and the Langmuir constant depending on the binding site affinity, respectively.

The Freundlich model is an empirical equation for multilayer adsorption and applied to heterogeneous adsorption sites. The model can be mathematically written as below:

$$q_e = K_F C_e^{1/n}$$

(4)

where K_F (mg/g) is a Freundlich constant indicative of the relative adsorption capacity of the adsorbent. and n is related to the adsorption capacity and adsorption favorability.

The Redlich-Peterson model has a hybrid feature of both Langmuir and Freundlich models and includes three adjustable parameters in an empirical isotherm model. The model can be typically applied in the following form:

$$q_e = \frac{K_R C_e}{1 + a_R C_e^{\alpha}}$$

(5)

where K_R (L/mg) and a_R (mg/L) are the Redlich-Peterson constants. And α is the exponent which lies between 0 and 1. when the value of $a_R C_e^{\alpha}$ is much bigger than 1, the above equation is reduced to the Freundlich isotherm. On the other hand, it is reduced to the Langmuir isotherm model, in case the value of the α is equal to 1.

Adsorption kinetics studies. NFC (0.05 g) was added into a glass bottle containing a stock solution of heavy metal ions (0.05 L, C_i = 50,000 ppm) and pH in the solution was not adjusted. Intervals of contact time were given between 1 and 1,200 min. The mixture was kept with agitation at 200 rpm and filtered. And then, the residual metal ion content in the solution was determined by using ICP-OES.

The sequestration kinetics of three heavy metal ions were fitted with pseudo-first-order, pseudo-second-order, and Elovich models. The pseudo-first-order kinetic model has an assumption that the sequestration rate is predominantly affected by the number of unoccupied adsorption sites. The equation can be given by:

$$q_t = q_e\left(1 - e^{-k_1 t}\right)$$

(6)

where q_t (mg/g) is the sequestration capacity at time t and k_1 is the rate constant of pseudo-first-order adsorption.

The pseudo-second-order model assumes that the sequestration has an assumption that the occupation rate of adsorption sites is proportional to the square of the number of the unoccupied adsorption site[1]. The model can be mathematically written as below:

$$q_t = \frac{k_2 q_e^2 t}{1 + k_2 q_e t}$$

(7)

where k_2 (g/mg·min) is the rate constant of pseudo-second-order adsorption.

The Elovich model can be used in case the adsorption is caused by chemisorption in highly heterogeneous adsorbent, and its rate decreases with increase of time because of covering of the surface. The Elovich model is given by:

$$q_t = \frac{1}{\beta}\ln(\alpha\beta) + \frac{1}{\beta}\ln t$$

(8)

where α (mg/g·min) is the initial adsorption rate and β (g/mg) is adsorption constant related to the extent of surface coverage and activation energy for chemisorption.

Multi-component batch sequestration experiments. NFC (0.1g) was added into a glass bottle containing a heavy metal (Pb^{2+}, Cu^{2+}, and Cd^{2+}) solution (0.1 L), as well as the four elements of Ca^{2+}, Mg^{2+}, Na$^+$, and K$^+$ (Ca(NO$_3$)·4H$_2$O, Mg(NO$_3$)$_2$·6H$_2$O, NaNO$_3$, and KNO$_3$, Sigma Aldrich, ≥99.0%) as interference elements. pH of the solution was not adjusted. The C_i of four interference elements was fixed at 100 mg/L, and the C_i of each three heavy metal ions

were adjusted in ratios to interference elements as 1:10, 1:5, 1:2, 1:1, 2:1, 5:1, and 10:1. The mixture was kept with agitation at 200 rpm for 24 h and filtered. Subsequently, the residual metal ion contents were determined by using ICP-OES.

Pressure drop tests in continuous flow process. In order to investigate effect of the sequestration capacity on the pressure drop, the pressure drop in the column packed with NFC was measured according to C_i and sequestration time for heavy metal ions. NFC (about 12g) was filled fully in a column with 1.5 cm-inner-diameter and 15 cm-length. Aqueous solution with differential C_i of heavy metal ions was circulated through the column from bottom to top with a linear flow rate of 1.4 m/s at room temperature for 1 h and water with C_i of 50,000 ppm for each heavy metal ions was circulated for 120 min. pH of the solution was not adjusted. The treated water was collected with intervals and filtered to determine the residual metal content of the solution by using ICP-OES.

In addition, the pressure drop by the NFC, as the flow rate of DI water increased, was compared with those of commercially available adsorbents. Polymer cation-exchanger (HCR-S, Dowex) is gel-type of styrene-DVB and has sulfonic acid group. The particle size was selected as 1 mm using a sieve. Also, the commercially available Zeolite 13X having similar diameter with NFC was obtained by Donggwang Co., Republic of Korea. And their porosity and average pore size were.

Effect of initial pressure on sequestration **processing efficiency.** In order to verify the effect of initial pressure in the inlet of column on sequestration capacities of the adsorbents (HCR-S, Zeolite 13X, and NFC), the aqueous solution with initial Cu^{2+} concentration of 50,000 ppm was pass through the adsorbents filled column, and circulated for 1 h with increase of initial pressure of the inlet of column. pH of the solution was not adjusted. The water samples were then collected and filtered to determine the residual metal ion contents by using ICP-OES.

The flows in the rectangular mesh-panel separation modules filled with HCR-S, Zeolite 13X, and NFC were numerically analyzed using the commercial computational fluid dynamics (CFD) code ANSYS CFX 18.2. The geometric parameters and operational conditions of the adsorbents and the adsorption modules were summarized in Supplementary Table 6 and 7 to conduct two-dimensional (2D) CFD models. Tetrahedral type mesh was generated with the ANSYS Design Modeler to analyze the separation module systems. The Reynolds-averaged Navier-Stokes (RANS) CFD approach was used to model and analyze the hydrodynamic behavior of water in the separation module, and the RANS equations were solved with the standard k-ε turbulence model with a scale wall function to describe detailed flow field characteristics around and in adsorbents. Each simulation was solved using convergence criteria based on a root mean square (RMS) residual of less than 1×10^{-4}. The obtained results with CFD analysis were compared to the experimental measurements.
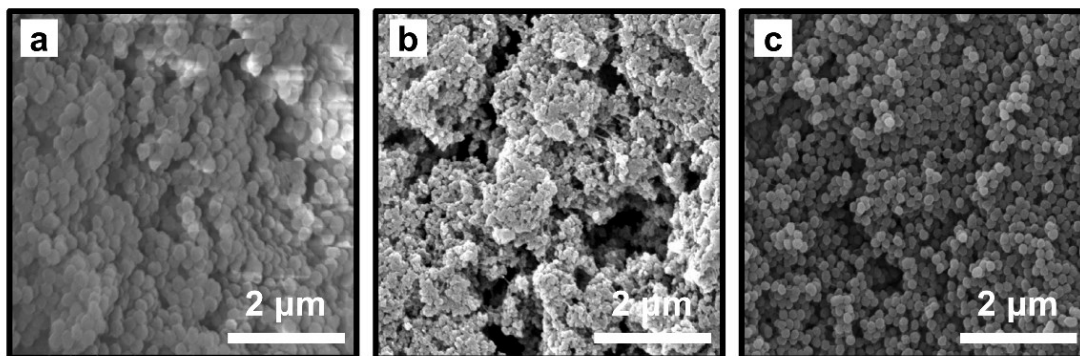
Fig. S1. SEM images of PAN-NPs according to the type of used surfactant in synthesis process. (a) Since the SDS tends to form tiny micelles of monomers, it can increase the particle number[3]. However, the synthesized PAN-NPs agglomerated due to their colloidal instability after polymerization. (b) NP-PEG-SO$_3$K, whose structure has repeating hydrophilic ether groups, was used for trying to enhance the dispersion stability of the PAN-NPs, however monomers clumped together due to its steric hindrance during polymerization. **c** Both SDS and NP-PEG-SO$_3$K were adopted to achieve the stably dispersed micelles by preventing the agglomeration of PAN-NPs, and allowed the fabrication of the well-monodispersed PAN-NPs with great reproducibility.
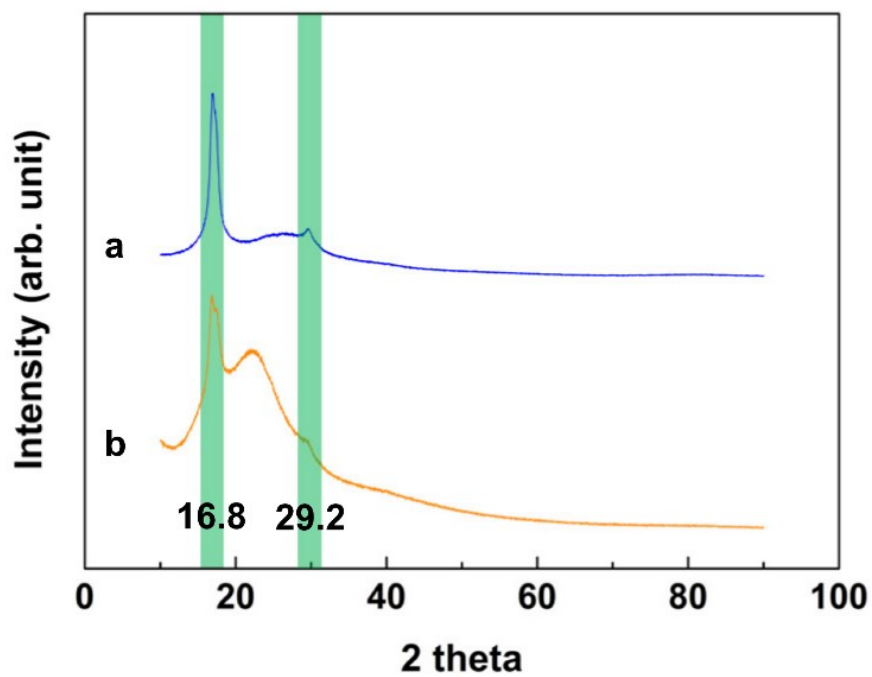
Fig. S2. XRD patterns of PAN-NP before and after amination. (a) Peaks of PAN-NP at 2 theta of 16.8 and 29.2 indicates a ordered rod-like molecular structure of PAN due to the intermolecular repulsion of the nitrile groups and (b) decreased after surface-amination.
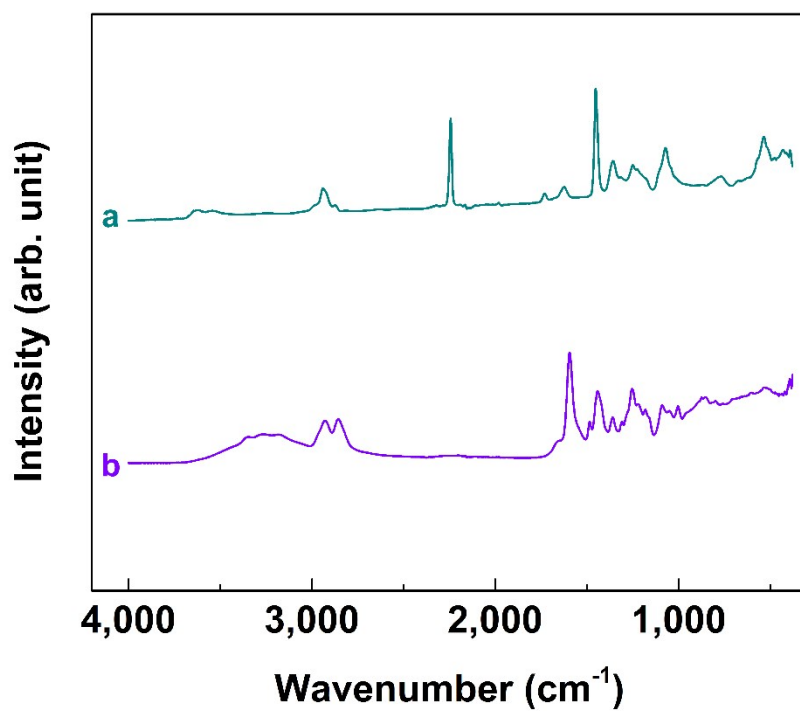
Fig. S3. FT-IR spectra of the synthesized PAN-NP and APAN-NP. Following peaks were assigned to specific functional groups of PAN-NP and APAN-NP. (a) Nitrile (C≡N) peak of PAN-NP at 2,250 cm^{-1}, and (b) amines (-NH- and -NH_2), amidine (N-C=N), -NH_2, and -NH- peaks of APAN-NP at 3500-2500 cm^{-1}, ~1638 cm^{-1}, 1600 cm^{-1}, and 1580 cm^{-1}.
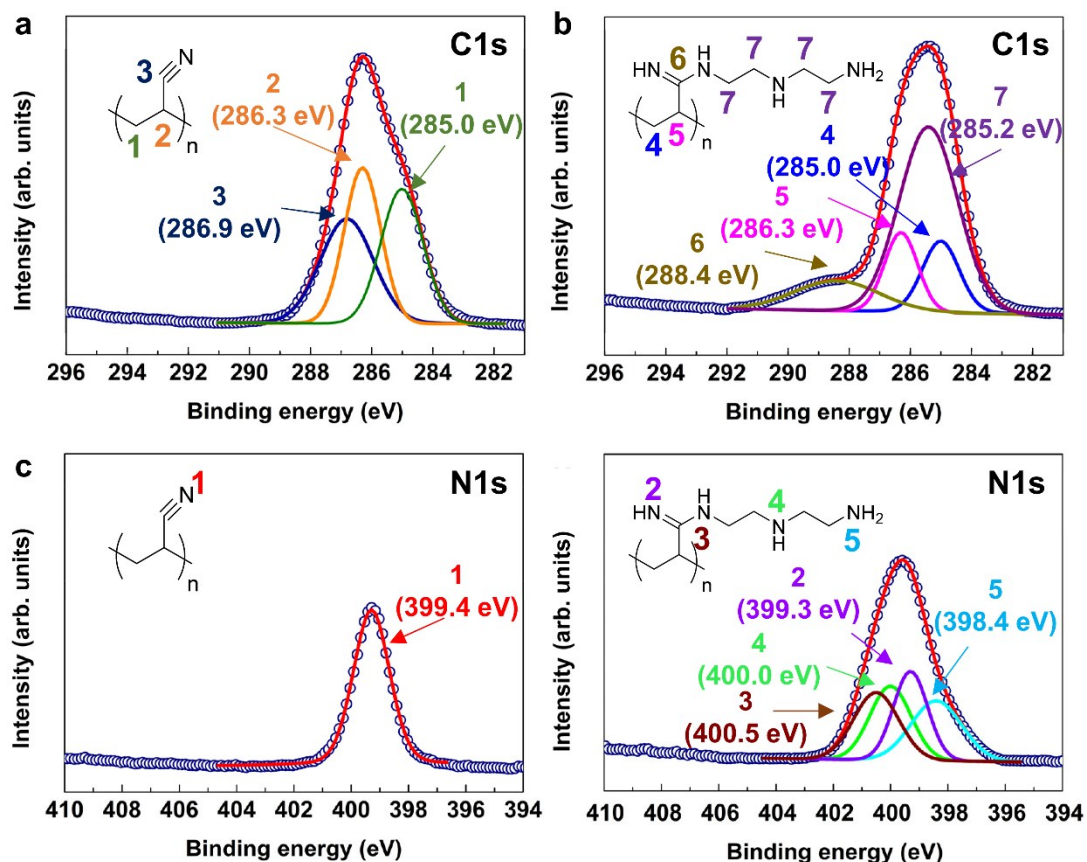
Fig. S4. XPS study for verifying the introduced amine-group onto PAN-NP. Deconvoluted XPS peaks of C1s and N1s high-resolution spectra for (a, c) PAN-NP and (b, d) APAN-NP were displayed. All binding energies were referenced to the neutral C 1s peak at 285.0 eV to compensate for the surface-charging effects. The deconvoluted C1s peaks of PAN-NPs appeared at binding energies[4] of 285.0 (C1), 286.3 (C2), and 286.9 (C3) eV. And deconvoluted peaks of APAN-NPs were assigned to the specific groups at binding energies[5,6] of 285.0 (C4), 286.3 (C5), 288.4 (C6), and 285.2 (C7) eV. The atomic ratios between deconvoluted peaks in the C1s spectra of the PAN-NP and APAN-NP were 1.00 (C1) : 1.01 (C2) : 0.99 (C3) and 1.00 (C4) : 0.95 (C5) : 1.01 (C6) : 4.11 (C7), and well matched with theoretical values of 1 : 1 : 1 and 1 : 1 : 1 : 4 for chemical groups in them, respectively. The deconvoluted N1s peaks of APAN-NPs appeared at binding energies of 400.5 (N2), 400.0 (N3), 399.3 (N4), and 398.4 (N5) eV[7,8]. The area ratio of deconvoluted peaks for N1s spectra of APAN-NP was 1.00 (N2) : 1.04 (N3) : 1.05 (N4) : 1.03 (N5).
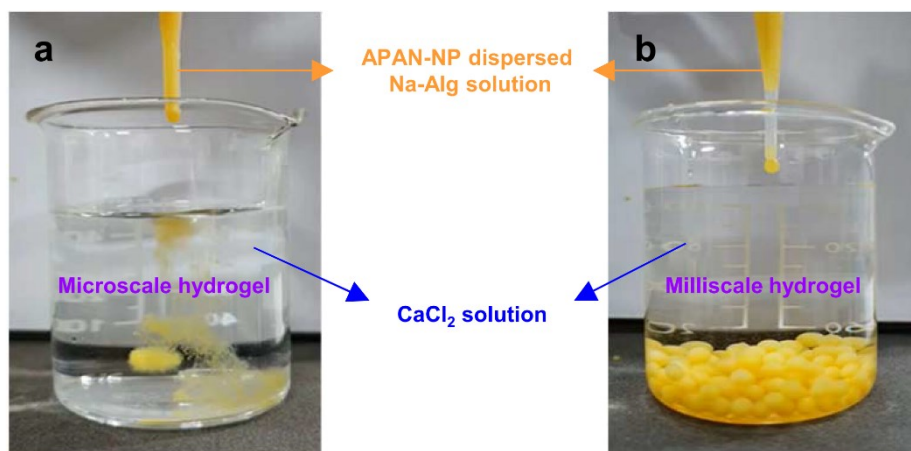
Fig. S5. Extrusion/external gelation of APAN-NP dispersed Na-Alg solution in 2 N CaCl$_2$ solution. (a) At higher content of APAN-NP than 95.7 wt%, millimeter-sized hydrogel preforms for the NFC adsorbents were produced. It suggests that the amount of Ca-Alg acting as a binder of APAN-NP was not enough for sufficient interconnection of APAN-NPs. (b) On the other hand, the millimeter-sized hydrogel, that we wanted, formed well at lower content of APAN-NP than 95.7 wt%.
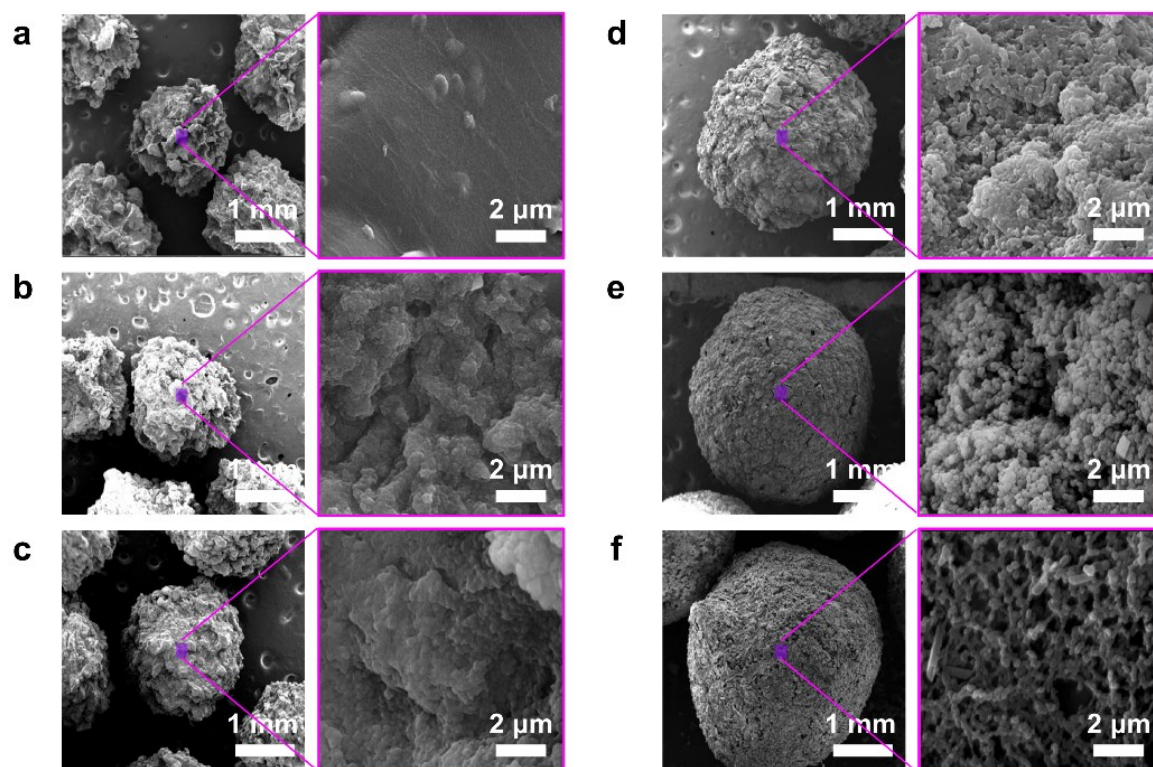
Fig. S6. SEM images of NFC adsorbents synthesized with various APAN-NP content. APAN-NP content in the adsorbents was (a) 0, (b) 10, (c) 20, (d) 50, (e) 80, and (f) 90 wt%. The nanofibrous-spherical structure formed at higher content of APAN-NP than 90 wt%.
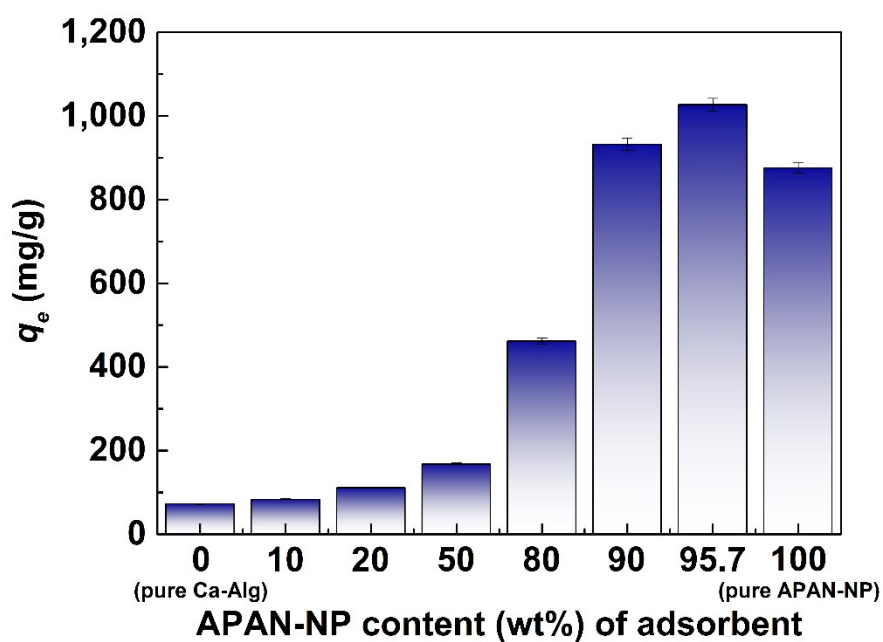
Fig. S7. sequestration capacity (Cu^{2+} solution of 50,000 mg/L) of adsorbents synthesized with various APAN-NP content. The NFC adsorbent synthesized with 95.7 wt% of APAN-NP showed the highest Cu^{2+} sequestration capacity. The sequestration capacities of the adsorbents at equilibrium increased exponentially with increase of the APAN-NP content. However, pure APAN-NP showed slightly lower sequestration capacity than the NFC adsorbent synthesized with 95.7 wt% of APAN-NP because it offered only surface of APAN-NP, not space in NFC for the crystal growth of Cu^{2+}.
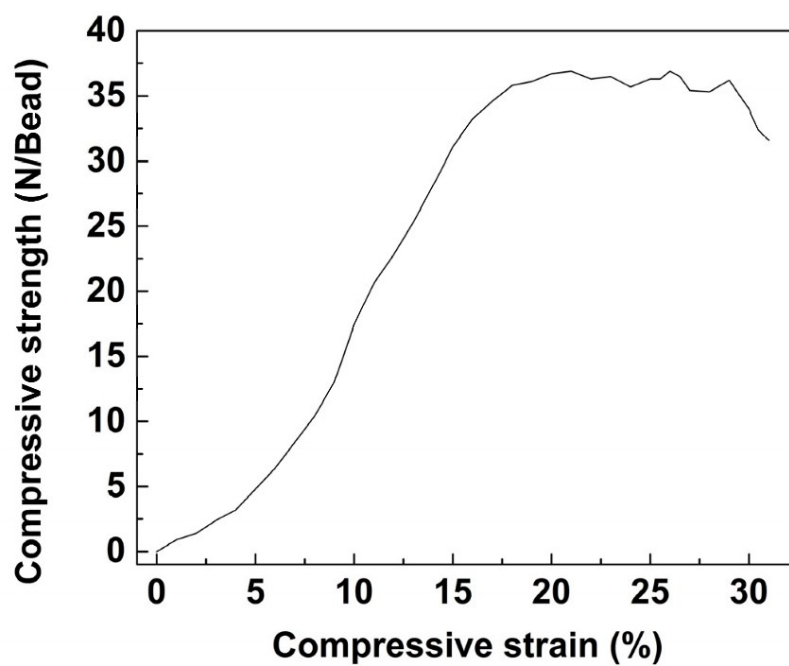
Fig. S8. The compressive stress-strain curve of the NFC adsorbent. The compressive strength of NFC increased nonlinearly up to ca. 20% of compressive strain. And then, the slightly tremble plateau region was observed between 20-27% due to the gradual destruction of the rigid nanofibrous structures of NFC.
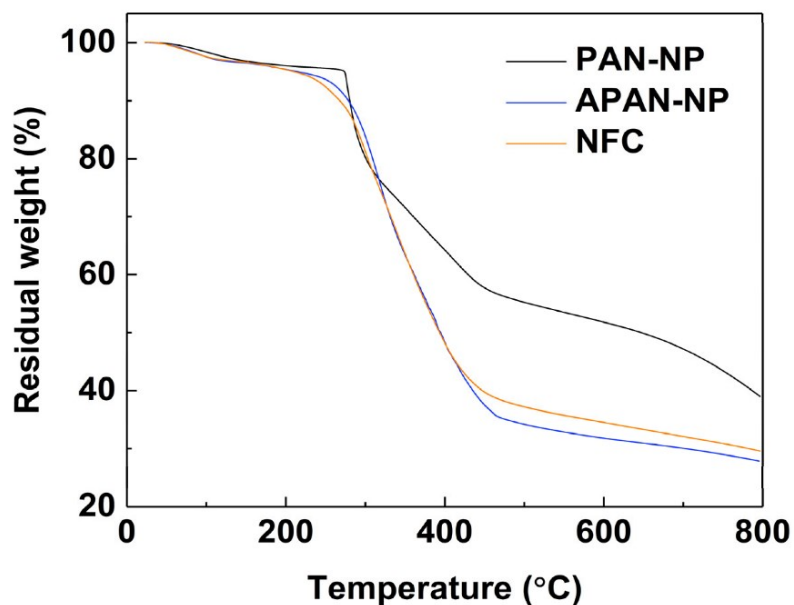
Fig. S9. TGA graphs of PAN-NP, APAN-NP, and NFC. Thermal behavior of materials in processing for preparing NFC were studied by TGA analysis in N_2 gas up to 800 °C at a heating rate 10 °C/min. TGA graph of NFC showed three major weight loss regions. The initial weight loss between 50 and 150 °C can be regarded to desorption of the physically absorbed water from the NFC. The second weight loss region between 270 and 460 °C can be ascribed as the thermal decomposition of amine-functionalized surface of PAN-NP. The third weight loss above 460 °C corresponds to the decomposition of PAN-NP.
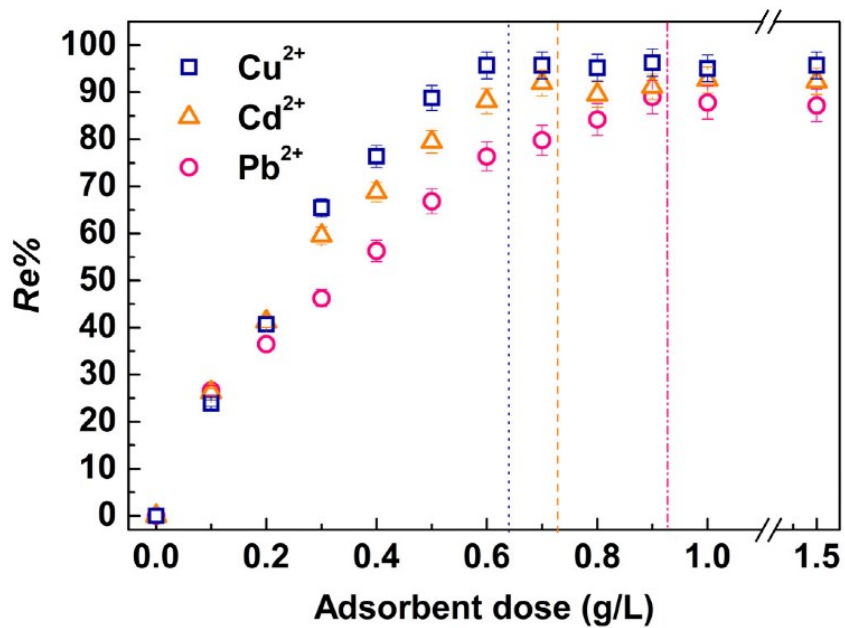
Fig. S10. Effect of adsorbent dose on *Re*% for Cu^{2+}, Cd^{2+}, and Pb^{2+}. As the adsorbent dose increased, the *Re*% for each heavy-metal ions reached to maximum of ~96% (Cu^{2+}), ~91% (Pb^{2+}), and ~90% (Cd^{2+}), and the order of maximum *Re*% for the three heavy-metal ions was opposite to that of adsorbent dose to reach maximum *Re*%.
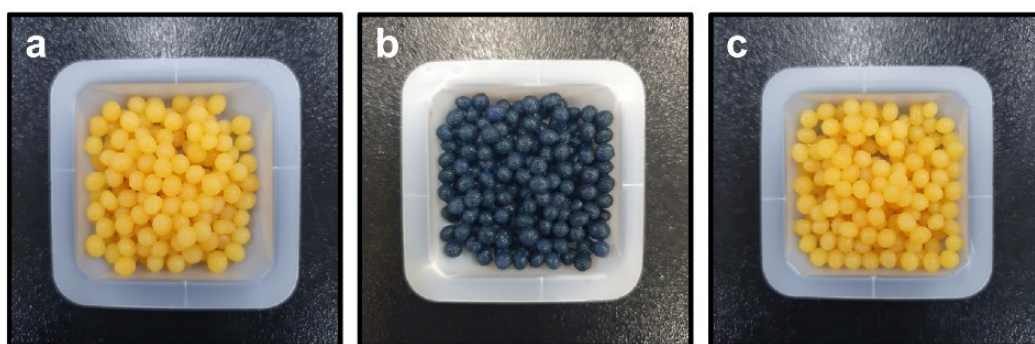
Fig. S11. Photographs for color changes of NFC adsorbents before and after regeneration. (a) pristine NFC, (b) NFC after sequestration of Cu^{2+}, and (c) regenerated NFC after 12 adsorption/desorption cycles.
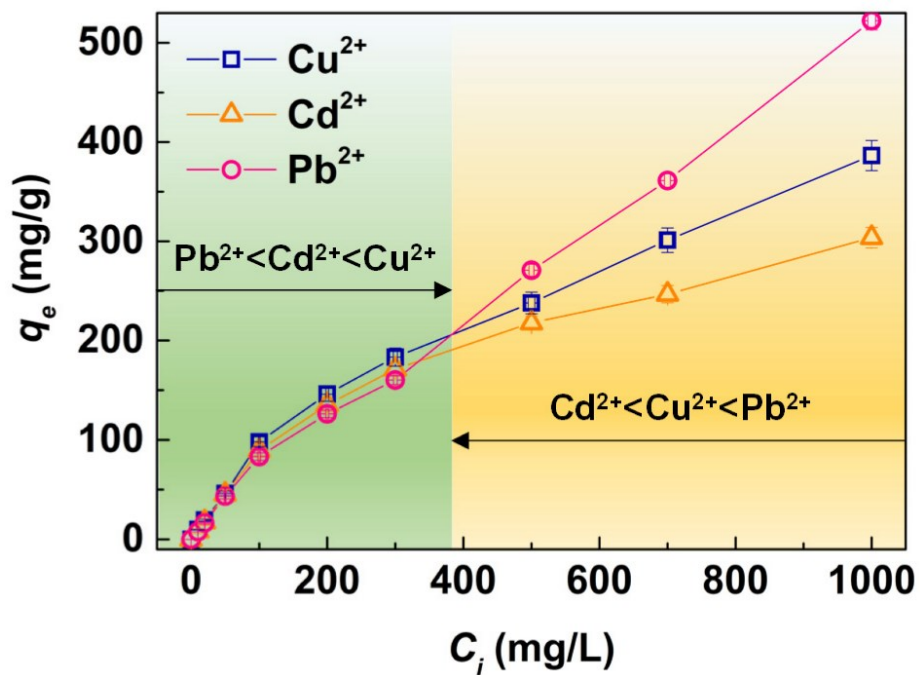
Fig. S12. Equilibrium sequestration capacity of NFC toward three heavy metal ions in a single batch adsorption system. The order of sequestration capacity of Cu^{2+}, Cd^{2+}, and Pb^{2+} for the NFC adsorbent changed from $Pb^{2+} < Cd^{2+} < Cu^{2+}$ to $Cd^{2+} < Cu^{2+} < Pb^{2+}$ at C_i of ca. 400 mg/L with increase of C_i.
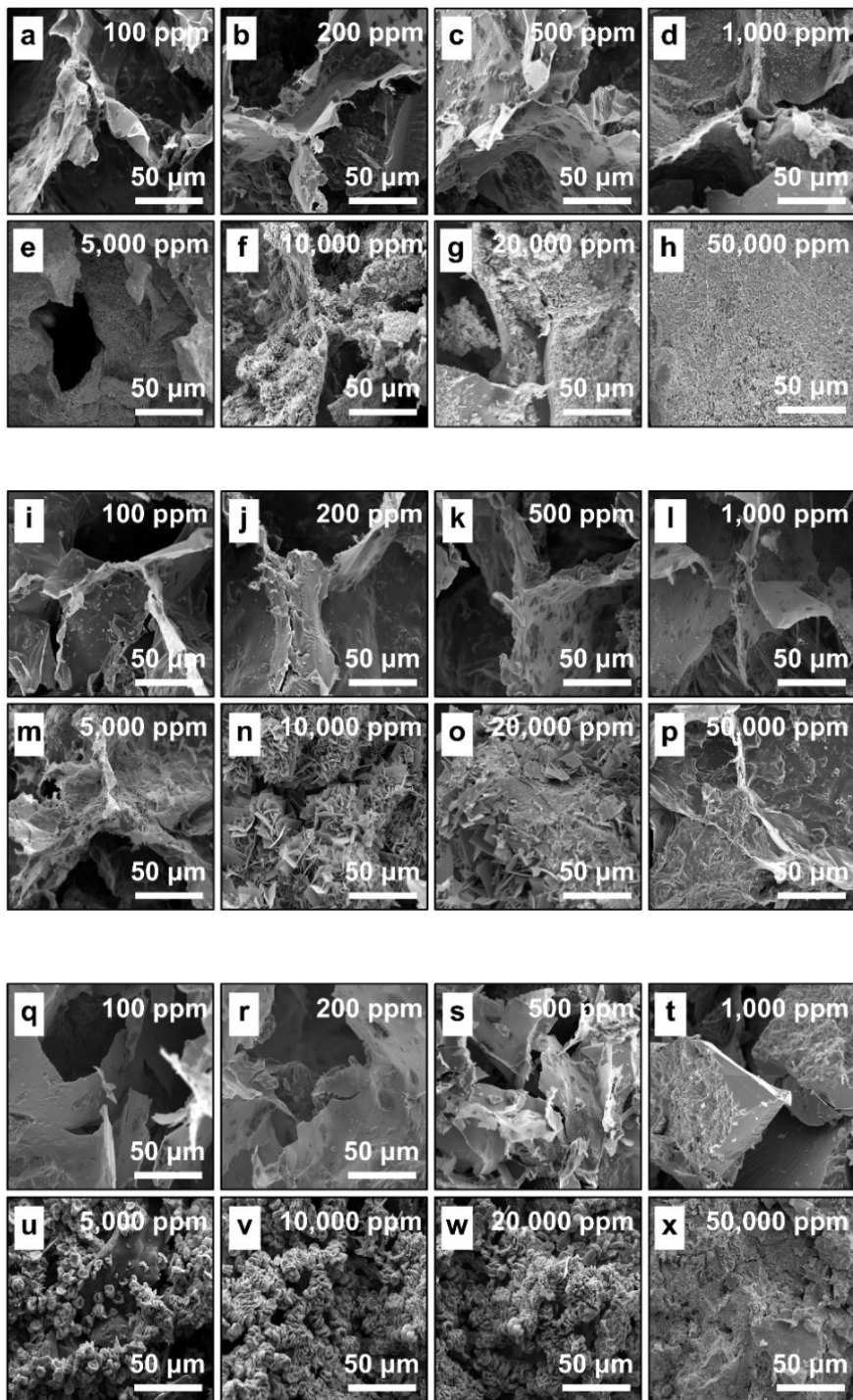
Fig. S13. SEM images for interior structures of NFC adsorbents after sequestration of heavy metal ions at various their concentrations. (a-h) Cu^{2+}. (i-p) Cd^{2+}, and (q-x) Pb^{2+}. The shapes of grown crystals from three heavy metal ions were obviously different from one another.
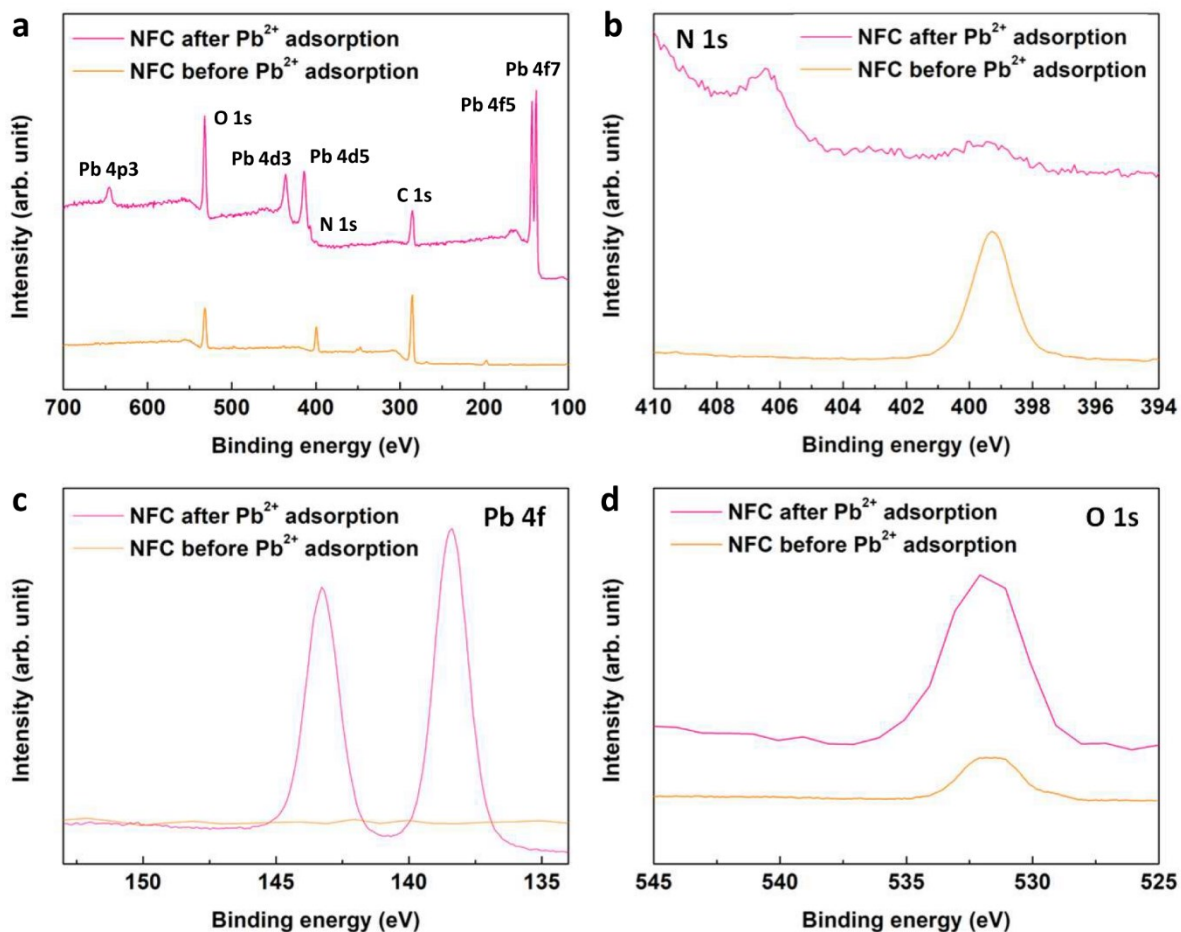
Fig. S14. XPS study for verifying the Pb^{2+} adsorption of NFC. (a) XPS survey spectra of NFC before and after Pb^{2+} adsorption. Deconvoluted XPS peaks of (b) N 1s, (c) Pb 4f, and (d) O 1s high-resolution spectra for NFC before and after Pb^{2+} adsorption. After Pb^{2+} adsorption, the new peaks related the adsorbed Pb. Moreover, the intrinsic C 1s, O 1s and N 1s peaks of NFC were changed. The C 1s and N 1s peaks decreased due to the thick lead crystal on the NFC surface. And the peaks at about 406.3 and 532 eV might be attributed to the anions such as NO_3^- and OH^- in the formed $Pb_4(NO_3)_4(OH)_4$ after Pb^{2+} adsorption. The metal peaks appeared distinctly after adsorption.
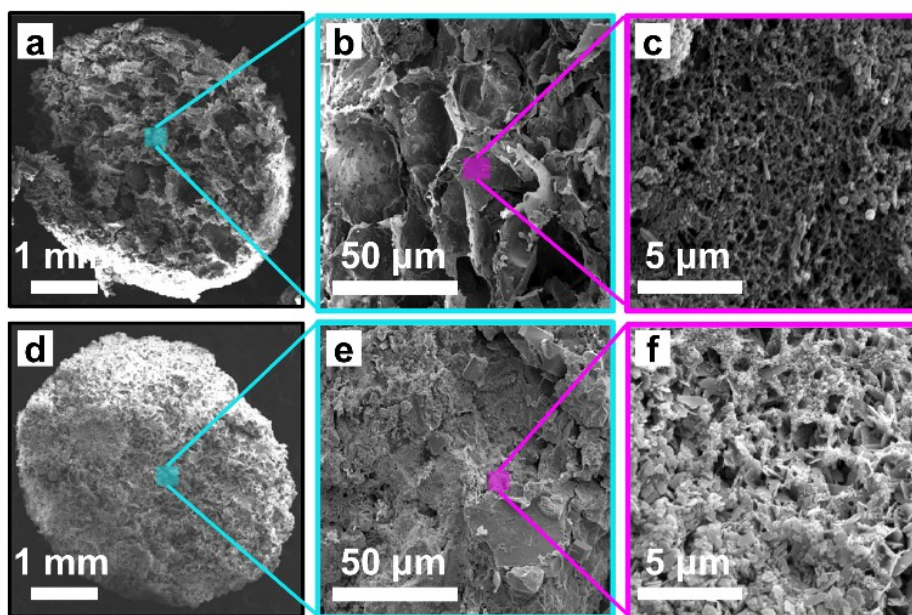
Fig. S15. SEM images of the hierarchically porous structures from low magnification to high magnification before and after Cu^{2+} sequestration on NFC adsorbents in C_i of 10,000 mg/L. (a-c) Hierarchically porous structure of the NFC adsorbent. Empty space inside NFC is attributed to the sublimation trace of ice during freeze-drying process, which provides enough space for crystal growth. (d-f) The grown crystal in the NFC adsorbent. The crystal grew perpendicular to the nano-fibrous structure and filled the inner space of NFC completely full.
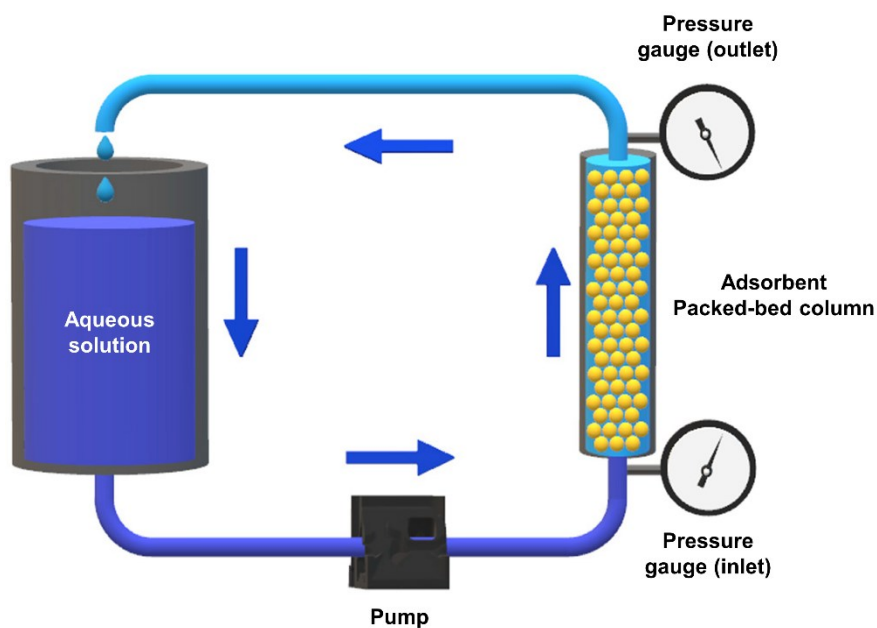
Fig. S16. Representative illustration for investigating pressure and sequestration efficiency in the column according to the flow rate. The pressure drop in the column filled with NFC was measured to investigate the effect of C_i and sequestration time on the pressure drop at 0.14 m/s of flow rate. In addition, the pressure differences between the inlet and outlet in column filled with adsorbents (HCR-S, Zeolite 13X, and NFC) were measured to investigate the effect of P_i on the pressure drop and sequestration performances with increasing flow rate of water from 0.01 to 0.25 m/s.
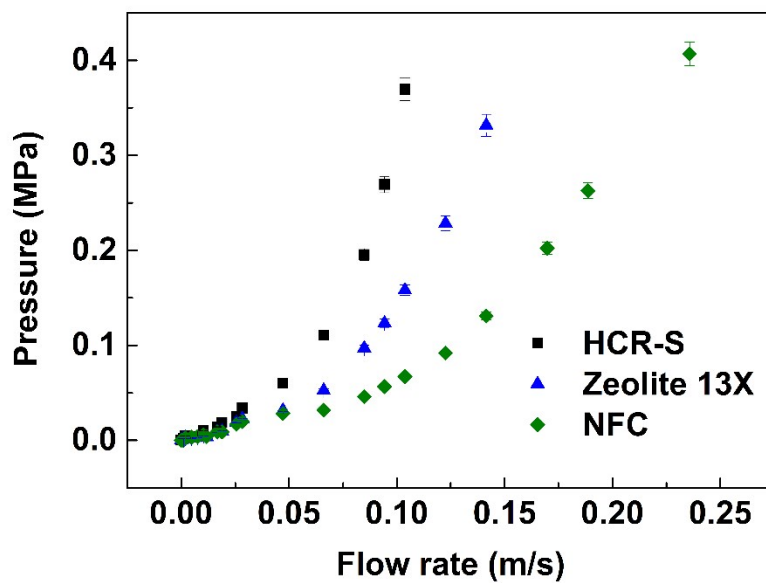
Fig. S17. Initial pressure values at the inlet of column packed with HCR-S, Zeolite 13X, and NFC, according to flow rate of water. Informations for HCR-S, Zeolite 13X, and NFC were summarized in Table S6. HCR-S and Zeolite 13X was selected for comparative analysis in consideration of their properties such as porosity, pore size, and particle size.
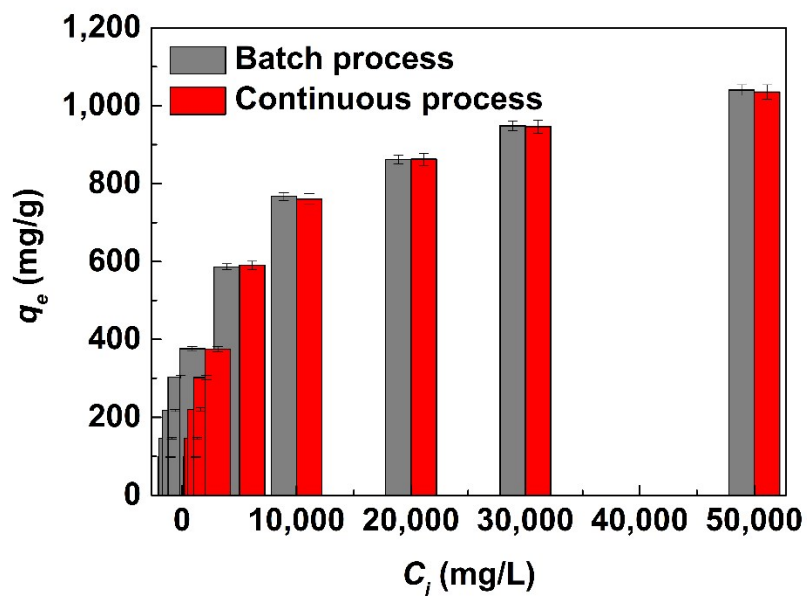
Fig. S18. Comparison of separation performance between batch and continuous processes according to initial concentration of $Cu(NO_3)_2$. The tests were carried out without pH adjustment of the solution for 1 hour at room temperature. The flow rate for the continuous process was ca. 0.14 m/s.
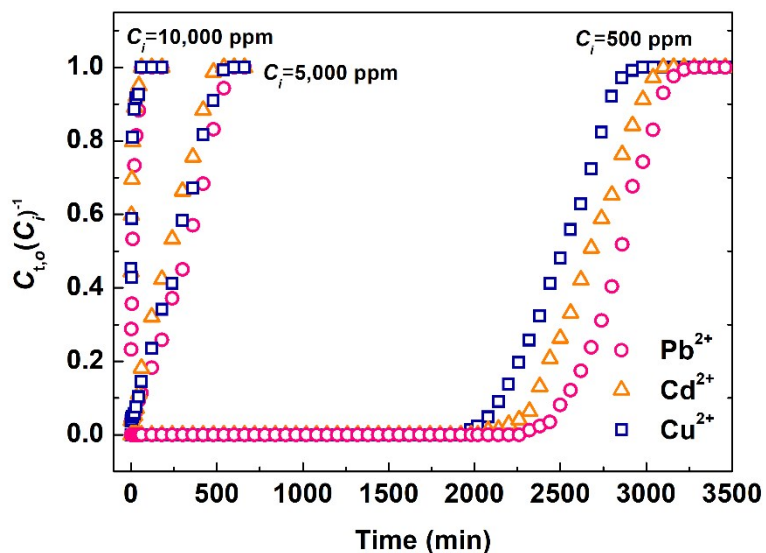
Fig. S19. Breakthrough curves for adsorption of Pb^{2+}, Cd^{2+}, and Cu^{2+} at different initial concentrations in NFC adsorption bed (flow rate is 0.17 m/s). The effect of the initial concentration on the breakthrough curve was investigated by adjusting the concentrations to 500, 10,000, and 20,000 mg/L at a constant flow rate of 0.17 m/s. The high-range concentration of heavy metal ions was employed in consideration of massive leakage accident of heavy metal ions. The NFC beds reached faster saturation with the increasing the initial concentration for all three metals. And, the exhaustion time and breakthrough decreased with the increasing initial concentrations, which can be attributed that higher initial concentrations resulted in higher driving force for mass transfer. On the other hand, a decrease of the initial concentration will lead to an extended breakthrough curve which exhibits higher volume of treated effluent for adsorption of heavy metal ions, because the lower concentration gradient may lead to a decrease in mass transfer coefficient or diffusion coefficient that yields a slower transportation of heavy metal ions into the adsorbent.
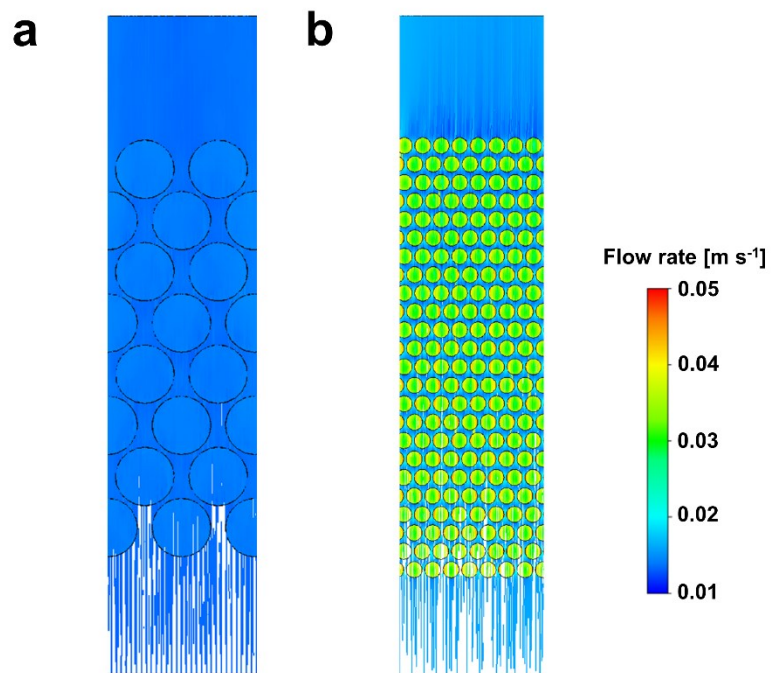
Fig. S20. Interpretation results of fluid flow in the separation modules filled with HCR-S and Zeolite 13X. 0.01 MPa of P_i at the inlet of column was applied to get simulations for the separation modules filled with (a) Zeolite 13X and (b) HCR-S. Zeolite 13X showed better penetration of fluid into its structure than HCR-S owing to a difference in the pore size.
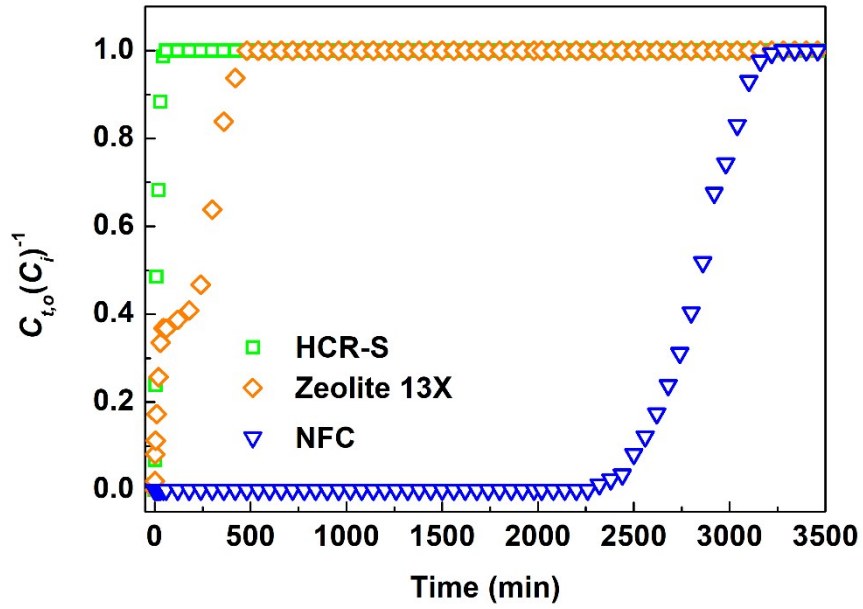
Fig. S21. Breakthrough curves for Pb^{2+} adsorption in the packed adsorption column with HCR-S, Zeolite 13X, and NFC (initial concentration is 500 mg/L, flow rate is 0.17 m/s).
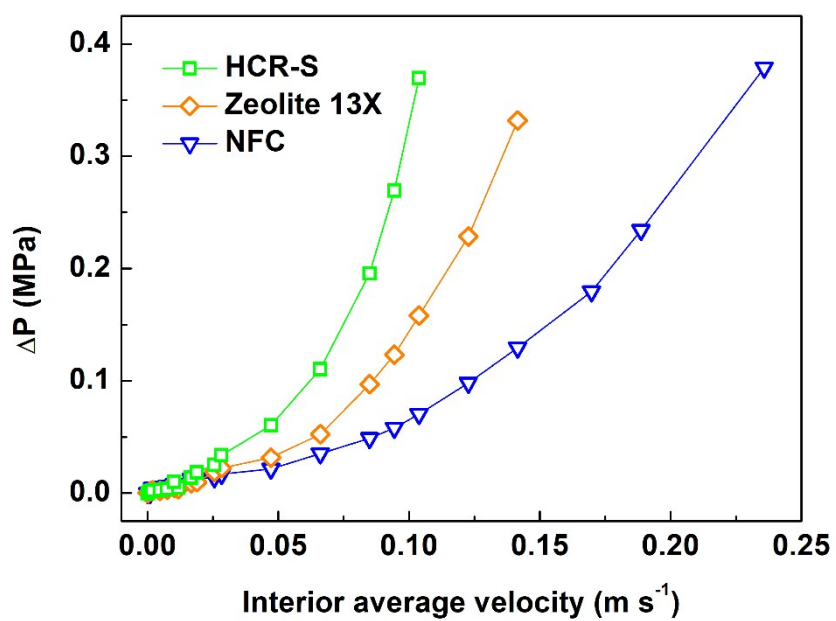
Fig. S22. The pressure drop values for HCR-S, Zeolite 13X, and NFC in the fixed-bed adsorption column, according to the interior average velocities.

Table S1. Synthesis conditions of NFC.

Conditions	Values and Methods
Ratio of APAN-NPs to Na-Alg	96:4
Concentration of Na-Alg solution	0.5 wt%
Average diameter of APAN-NPs	235 nm
Dispersion method of APAN-NPs in Na-Alg sol.	Ultra-sonication
Injection rate of APAN-NP dispersed sol.	15 mL/min
Nozzle tip diameter	2 mm
Gap between nozzle tip and surface of gelation bath	50 mm
Concentration of $CaCl_2$ solution	2 N
Gelation temperature	25 °C
Gelation time	3 h
Washing solution	1:1 ratio of water/ethanol
Drying method for NFC	Rapid refrigeration and freeze-drying

Table S2. Measured pH values of solution according to C_i of three heavy metal ions.

C_i (mg/L)	pH		
	Pb^{2+}	Cu^{2+}	Cd^{2+}
1	6.59	6.57	6.73
2	5.91	5.78	6.70
5	5.49	5.66	6.65
10	5.38	5.45	6.64
20	5.35	5.39	6.42
50	5.29	5.23	6.29
100	5.27	5.19	6.23
200	5.09	4.98	5.93
500	4.91	4.76	5.81
1,000	4.68	4.65	5.74
2,000	4.56	4.34	5.56
5,000	4.53	4.01	5.50
10,000	4.48	3.88	5.39
20,000	4.02	3.51	5.21
50,000	3.62	2.81	4.60

Table S3. Final concentrations of three heavy metal ions according to C_i after sequestration using NFC

C_i (mg/L)	C_f (µg/L)		
	Pb^{2+}	Cu^{2+}	Cd^{2+}
1	0.1	0.1	0
2	0.1	0	0
5	0	0	0.1
10	0	0	0
20	0.1	0.1	0
50	1.1	0.1	0.1

Table S4. List of references for Fig. 2d. Information on maximum sequestration capacity, size of adsorbent, and sequestration mechanism for supplementary references.

Supplementary reference	q_m (mg/g)			Adsorbent diameter	Adsorbent	Sequestration mechanism
	Cd^{2+}	Cu^{2+}	Pb^{2+}			
9	-	111	78	~300 nm	Polypyrrole/MoS_4^{2-} composite	Ion-exchange,
10	47	32	106	10-40 nm	Attapulgite/carbon composite	Electrostatic interaction, Surface complexation
11	633	260	-	280-360 nm	Cubic mesoporous silica modified with 2,2'-(((((3-(triethoxysilyl)propyl)azanediyl)bis(methylene))bis(2,1-phenylene))bis(oxy))bis(N-(4-((E)-phenyldiazenyl)phenyl)acetamide)	Chelation
12	128	-	385	~ 220 nm	Fe_3O_4/SiO_2/graphene oxide/n-propyl trimethoxy silane	Ion-exchange Chelation
13	95	-	140	~260 nm	Poly(maleic anhydride)-graft-Poly(vinyl alcohol) comb polymer Functionalized magnetic nanoparticles	Stimuli-responsive
14	-	336	254	~7 nm	Ultrathin Zn(Bim)(OAc) nanosheet	Chelation
15	193	-	761	~250 nm	Phosphated titanium oxide with amino and hydroxyl bifunctional groups	Chelation
16	476	526	556	~269 nm	Polystyrene-poly(N-isopropylmethacrylamide-acrylic acid) core/shell gel particles	Ion-exchange, Chelation
17	-	92	113	~20 nm	Chitosan/Fe_3O_4 nanopowder	Chelation
18	-	109	455	~800 nm	Graphene oxide functionalized with	Chelation

ethylenediamine triacetic acid

19	345	-	465	~30 nm	Carboxylated cellulose nanocrystals	Ion-exchange, Chelation
20	357	161	94	~500 nm	Poly(ether sulfones)/poly(ethyleneimine)	Chelation,
21	95	88	113	55-65 nm	magnetite nanorods	Electrostatic force
22	-	204	565	~90 nm ~70 nm	Layered Titanate Nanostructure	Ion-exchange
23	446	524	369	~70 nm	Amine-functionalized mesoporous Fe_3O_4 nanoparticle	Chelation
24	166	218	559	Less than 1,000 nm	Micro-nano-engineered nitrogenous bone biochar	Cation ion exchange, Electrostatic interaction, Surface complexation
25	106	-	257	30-135 nm	Lignin-based magnesium hydroxide nanocomposite	Ion-exchange
26	75	-	311	250-500 µm	Contrasting biochars	Cation release
27		146	272	2 µm	Poly(aminopropyl/methyl)silsesquioxane particles	Chelation
28	9	8	-	~ 550 µm	Biopolymer template synthesized mesoporous titania beads	Electrostatic Interaction
29	42	-	316	10-100 µm	Oxygen-doped bundlelike porous boron nitride	Chelation
30	151	-	295	~60 µm	Microwave-functionalized cellulose	Ion-exchange, Chelation, Physical adsorption
31	-	19	10	Microscale	2-imino-4-thiobiuret–partially reduced graphene oxide	Chelation
32	202		239	3.04 µm	Chitosan microsphere grafted by methyl acrylate and diethylenetriamine	Chelation
33	33	24	54	Microscale	Bio-inspired surface-functionalization of graphene oxide	Chelation

34	50	47	47	80 μm	Ca (II) imprinted chitosan microsphere	Ion-exchange, Chelation
35	59	80	434	Microscale	Iron oxide nano-particles-immobilized-sand material	Ion-exchange
36	103		101	Milliscale	Multithiol functionalized graphene bio-sponge	Ion-exchange, Chelation
37	137		256	Milliscale	Sponge-like polysiloxane-graphene oxide gel	Chelation
38	94	54	202	Milliscale	Hydrogel-supported nanosized hydrous manganese dioxide	Ion-exchange
39	18	9	34	10×40×5 mm^3	Poly(HEA/MALA) hydrogel	Ion-exchange Chelation
40	27	15	39	Milliscale	Sulfhydryl functionalized hydrogel with magnetism	Ion-exchange Chelation
41	86	99	138	12×12×5 mm^3	EDTA functionalized chitosan/polyacrylamide double network hydrogel	Ion-exchange
42	4	6	9	10 mm	Poly (vinyl alcohol) and carboxymethyl cellulose composite hydrogels	Ion-exchange
43	154		216	Milliscale	Polyampholyte hydrogel	Ion-exchange Complexation
44	131	106	126	Milliscale	2-acrylamido-2-methyl-1-propansulfonic acid magnetic hydrogel	Ion-exchange
45	116		195	Milliscale	Alcohol/polyacrylic acid double network gel	Ion-exchange Chelation
46	98	92	226	2.44 mm	Alginate/polyethyleneimine	Chelation
this work	1040	1204	1891	4.05 mm	Nanofibrous-spherical cage (NFC) adsorbent	Chelation and Crystal growth (Surface-precipitation)

Table S5. Model parameters of three isotherm models for heavy metal ions.

	Langmuir			Freundlich			Redlich-Peterson			
	q_m	K_L (×10⁻⁴)	R^2	n	K_F	R^2	K_R	α	a_R	R^2
Pb^{2+}	1909.431	1.877	0.940	2.987	49.461	0.986	4.638	0.703	0.0627	0.998
Cu^{2+}	1016.473	0.614	0.931	3.659	59.423	0.976	3.129	0.796	0.0257	0.986
Cd^{2+}	876.724	0.657	0.833	3.843	58.756	0.979	7.419	0.762	0.104	0.989

Table S6. Model parameters of three kinetic models for heavy metal ions.

	Pseudo-first order			Pseudo-second order			Elovich		
	q_e (×10²)	k_1	R^2	q_e (×10²)	k_2 (×10⁻³)	R^2	α	β	R^2
Pb^{2+}	17.841	0.429	0.935	19.019	3.175	0.989	2.227	161.034	0.866
Cu^{2+}	11.130	0.298	0.930	11.918	4.143	0.984	7.707	67.291	0.912
Cd^{2+}	10.102	0.088	0.946	10.620	1.412	0.985	0.116	120.632	0.880

Table S7. k_2 comparison of NFC for heavy metal ions with other millimeter-sized adsorbents.

Supple-mentary reference	k_2 ($\times 10^{-3}$)		
	Cd^{2+}	Cu^{2+}	Pb^{2+}
36	5.81	-	1.62
37	0.80	-	1.80
38	0.50	0.49	0.23
39	0.65	0.73	0.30
40	0.33	0.68	0.13
41	1.02	1.25	0.44
43	4.90	-	8.10
45	0.17	-	0.74
This work	1.41	4.14	3.18

Table S8. Structural properties of NFC, Zeolite 13X, and HCR-S.

Sample	Average pore size (μm)	Porosity (mL/g)	Average diameter (mm)
NFC	32.22	0.76	4.01
Zeolite 13X	0.24	0.28	3.99
HCR-S	0.00045[47]	0.000077[47]	1.07

Table S9. Geometrical parameters and operational conditions.

Geometry	
Column diameter (m)	0.015
Column length (m)	0.15
Boundary condition for NFC	
Fluid	Water
Inlet pressure (MPa)	0-0.4
Mass flow rate (kg/s)	0-0.04
Boundary condition for Zeolite 13X	
Fluid	Water
Inlet pressure (MPa)	0-0.4
Mass flow rate (kg/s)	0-0.03
Boundary condition for HCR-S	
Fluid	Water
Inlet pressure (MPa)	0-0.4
Mass flow rate (kg/s)	0-0.02
Mesh number information	
Number of meshes for NFC	38025
Number of meshes for Zeolite 13X	38025
Number of meshes for HCR-S	643122

Table S10. Comparison of pressure drop between results obtained from CFD analyses and experiments.

Adsorbent	Initial pressure (MPa)	Mass flow rate (kg/s)	Pressure drop obtained from CFD analysis (MPa)	Pressure drop obtained from experiment (MPa)
HCR-S	0.01	0.002	0.013	0.010
	0.11	0.012	0.079	0.075
	0.20	0.015	0.133	0.127
	0.27	0.017	0.162	0.154
	0.37	0.018	0.221	0.206
Zeolite 13X	0.01	0.003	0.009	0.008
	0.10	0.015	0.058	0.055
	0.16	0.018	0.092	0.089
	0.23	0.022	0.134	0.129
	0.33	0.025	0.180	0.174
NFC	0.01	0.004	0.007	0.006
	0.09	0.022	0.058	0.055
	0.2	0.030	0.108	0.101
	0.26	0.033	0.139	0.131
	0.41	0.042	0.222	0.212

Supplementary References

1.   Chen, Z., Ma, W. & Han, M., *J. Hazard. Mater.*, 2008, **155**, 327-333.

2.   ANSYS CFX-solver theory guide., *ANSYS CFX Release*, 2009, **15317**, 724-746.

3.   Flockhart, B., *J. Colloid. Sci.*, 1957, **12**, 557-565.

4.   Ko, Y. G. *et al.*, *J. Hazard. Mater.*, 2016, **307**, 91-98.

5.   Zhao, R., Li, X., Sun, B., Ji, H. & Wang, C., *J. Colloid Interface Sci.*, 2017, **487**, 297-309.

6.   Shen, L. Y., Shen, L., Wang, Z. X. & Chen, L. Q., *ChemSusChem*, 2014, **7**, 1951-1956.

7.   Marzorati, S., Ragg, E. M., Longhi, M. & Formaro, L., *Mater. Chem. Phys.*, 2015, **162**, 234-243.

8.   Mian, M. M. et al., *Chemosphere*, 2018, **208**, 712-721.

9.   Xie, L. X. et al., *Adv. Funct. Mater.*, 2018, **28**, 1800502.

10.   Tang, J., Mu, B., Zheng, M. S. & Wang, A. Q., *ACS Sustain. Chem. Eng.*, 2015, **3**, 1125-1135.

11.   Chatterjee, S. & Paital, A. R., *Adv. Funct. Mater.*, 2018, **28,** 1704726.

12.   Bao, S. Y., Yang, W. W., Wang, Y. J., Yu, Y. S. & Sun, Y. Y., *J. Hazard. Mater.*, 2020, **381,** 120914.

13.   Liu, X. et al., *J. Clean Prod.*, 2020, **253,** 119915.

14.   Xu, R. M. et al., *Chem. Eng. J.*, 2020, **382,** 124844.

15.   Wang, P. et al., *Environ.-Sci. Nano*, 2020, **7**, 1266-1274.

16.   Naseem, K. et al., *J. Mol. Liq.*, 2019, **277**, 522-531.

17.   Pu, S. Y. et al., *ACS Sustain. Chem. Eng.*, 2018, **6**, 16754-16765.

18.   Carpio, I. E. M., Mangadlao, J. D., Nguyen, H. N., Advincula, R. C. & Rodrigues, D. F., *Carbon*, 2014, **77**, 289-301.

19.   Yu, X. L. et al., *J. Environ. Sci.*, 2013, **25**, 933-943.

20.   Min, M. H. et al., *Chem. Eng. J.*, 2012, **197**, 88-100.

21.   Karami, H., *Chem. Eng. J.*, 2013, **219**, 209-216.

22.   Li, N. et al., *Adv. Funct. Mater.*, 2012, **22**, 835-841.

23.   Xin, X. et al., *Chem. Eng. J.*, 2012, **184**, 132-140.

24.   Xiao, J., Hu, R. & Chen, G. C., *J. Hazard. Mater.*, 2020, **387,** 121980.

25.   Ponomarev, N., Pastushok, O., Repo, E., Doshi, B. & Sillanpaa, M., *ACS Appl. Nano Mater.*, 2019, **2**, 5492-5503.

26.   Trakal, L., Bingol, D., Pohorely, M., Hruska, M. & Komarek, M., *Bioresour. Technol.*, 2014, **171**, 442-451.

27.   Lu, X., Yin, Q. F., Xin, Z., Li, Y. & Han, *J. Hazard. Mater.*, 2011, **196**, 234-241.

28.   Wu, N., Wei, H. H. & Zhang, L. Z. *Environ. Sci. Technol.*, 2012, **46**, 419-425.

29.   Liu, F. et al., *ACS Sustain. Chem. Eng.*, 2018, **6**, 16011-16020.

30.   Qu, J. H. et al., *J. Hazard. Mater.*, 2020, **387,** 121718.

31.   Awad, F. S., AbouZeid, K. M., El-Maaty, W. M. A., El-Wakil, A. M. & El-Shall, M. S., *ACS Appl. Mater. Interfaces*, 2017, **9**, 34230-34242.

32.   Zhang, H. et al., *ACS Appl. Mater. Interfaces*, 2017, **9**, 11144-11155.

33.   Dong, Z. H. et al., *J. Mater. Chem. A*, 2014, **2**, 5034-5040.

34.   He, J., Lu, Y. & Luo, G., *Chem. Eng. J.*, 2014, **244**, 202-208.

35.   Lee, S. M., Laldawngliana, C. & Tiwari, D., *Chem. Eng. J.*, 2012, **195**, 103-111.

36.   Yap, P. L. et al., *Chem. Eng. J.*, 2020, **395** 124965.

37.   Zhou, G. Y. et al., *Chem. Eng. J.*, 2015, **280**, 275-282.

38.   Zhu, Q. & Li, Z. K., *Chem. Eng. J.*, 2015, **281**, 69-80.

39.   Wu, N. M. & Li, Z. K., *Chem. Eng. J.*, 2013, **215**, 894-902.

40.   Hua, R. & Li, Z. K., *Chem. Eng. J.*, 2014, **249**, 189-200.

41.   Ma, J. et al., *ACS Sustain. Chem. Eng.*, 2017, **5**, 843-851.

42.   Wang, L.-Y. & Wang, M.-J., *ACS Sustain. Chem. Eng.*, 2016, **4**, 2830-2837.

43.   Zhou, G. Y. et al., *Water Res.*, 2016, **89**, 151-160.

44.   Ozay, O., Ekici, S., Baran, Y., Aktas, N. & Sahiner, N., *Water Res.*, 2009, **43**, 4403-4411.

45.   Chu, L. et al., *J. Hazard. Mater.*, 2015, **300**, 153-160.

46.   Demey, H., Vincent, T. & Guibal, E., *Chem. Eng. J., 2018,* **332**, 582-595.

47.   Yang, J. I. et al., *Can. J. Chem. Eng.*, 2007, **85**, 83-91 (2007).